

# B-mode forecast of CMB-Bhārat

Debabrata Adak<sup>1\*</sup>, Aparajita Sen<sup>2†</sup>, Soumen Basak<sup>2</sup>, Jacques Delabrouille<sup>3,4,5</sup>,  
Tuhin Ghosh<sup>6</sup>, Aditya Rotti<sup>7</sup>, Ginés Martínez-Solaesche<sup>8</sup>, Tarun Souradeep<sup>10,9,1</sup>

<sup>1</sup> *Inter University Centre for Astronomy and Astrophysics, Post Bag 4, Ganeshkhind, Pune-411007, India*

<sup>2</sup> *School of Physics, Indian Institute of Science Education and Research Thiruvananthapuram, Maruthamala PO, Vithura, Thiruvananthapuram 695551, Kerala, India*

<sup>3</sup> *APC, CNRS/IN2P3, Université Paris Diderot, 10, rue Alice Domon et Léonie Duquet, 75205 Paris Cedex 13, France,*

<sup>4</sup> *IRFU, CEA, Université Paris Saclay, 91191 Gif-sur-Yvette, France*

<sup>5</sup> *Department of Astronomy, School of Physical Sciences, University of Science and Technology of China, Hefei, Anhui 230026, China.*

<sup>6</sup> *School of Physical Sciences, National Institute of Science Education and Research, HBNI, Jatni 752050, Odisha, India*

<sup>7</sup> *Jodrell Bank Centre for Astrophysics, School of Physics and Astronomy, The University of Manchester, Oxford Road, Manchester, M13 9PL, U.K.*

<sup>8</sup> *Instituto de Astrofísica de Andalucía (CSIC), PO Box 3004, 18080 Granada, Spain*

<sup>9</sup> *Indian Institute of Science Education and Research, Dr. Homi Bhabha Road, Pashan, Pune 411008, Maharashtra, India*

<sup>10</sup> *Raman Research Institute, C. V. Raman Avenue, Bengaluru, Karnataka 560080, India*

Accepted – Received

## ABSTRACT

Exploring Cosmic History and Origins (ECHO), popularly known as ‘CMB-Bhārat’, is a space mission that has been proposed to the Indian Space Research Organisation (ISRO) for the scientific exploitation of the Cosmic Microwave Background (CMB) at the next level of precision and accuracy. The quest for the CMB polarization *B*-mode signals, generated by inflationary gravitational waves in the very early universe, is one of the key scientific goals of its experimental design. This work studies the potential of the proposed ECHO instrumental configuration to detect the target tensor-to-scalar ratio  $r \sim 10^{-3}$  at  $3\sigma$  significance level, which covers the predictions of a large class of inflationary models. We investigate the performance of two different component separation pipelines, NILC and Commander, for the measurement of  $r$  in presence of different physically motivated models of astrophysical foregrounds. For a simplistic foreground model (only polarized dust and synchrotron), both component separation pipelines can achieve the desired sensitivity of ECHO, i.e.  $\sigma(r=0) \sim (0.4 - 0.7) \times 10^{-3}$ . NILC performs better than Commander in terms of bias on recovered  $r$  for complex spectral models (power-law and curved power-law) of the synchrotron emission and complex dust models (dust decorrelation). Assuming 84% delensing, we can achieve an improvement of  $\sigma(r=0)$  by approximately 50% as compared to the results obtained for the same configuration without any lensing correction.

**Key words:** Cosmology: observations — methods: data analysis — Polarization — cosmic background radiation — diffuse radiation — inflation.

## 1 INTRODUCTION

The Cosmic Microwave Background (CMB) provides direct information about the earliest moments of our universe, and our current understanding about the origin and the subsequent cosmological evolution of the universe is heavily based on measurements of this relic radiation. Over the last couple of decades, a huge amount of information has been accumu-

lated about the temperature and polarization anisotropies of CMB. Ground-based, Balloon-borne and Satellite missions (Planck Collaboration et al. 2011; Ade et al. 2014; Aiola et al. 2020; Choi 2020; Sayre et al. 2020; Gualtieri et al. 2018; Aghanim et al. 2020) have measured the CMB anisotropies at various angular scales and frequencies. All these observations have successfully converged into the  $\Lambda$ CDM model, or concordance cosmology (See Bull et al. (2016) for review): a spatially flat expanding universe composed of matter, baryons and vacuum energy with a nearly scale-invariant spectrum of primordial fluctuations. The global properties

\*E-mail: debabrata@iucaa.in

†aparajita15@iisertvm.ac.in

of the universe are characterized by the density of baryons, cold dark matter and dark energy. Primordial perturbations of the space-time metric, i.e. the initial conditions for our observable universe, are thought to originate from a phase of cosmic inflation (Starobinsky 1980; Kazanas 1980; Guth 1981; Sato 1981; Linde 1982; Albrecht & Steinhardt 1982). During this epoch, the universe is stretched so violently that tiny quantum fluctuations are imprinted on cosmological distance scales. These fluctuations grow over the time due to gravitational instability to give all the large scale structure that we observe today.

A generic prediction of inflationary models is the generation of a stochastic background of gravitational waves, the ripples in the fabric of space-time, which gives rise to a faint but distinctive twisting pattern in the polarization of the CMB, known as *B*-modes (Seljak & Zaldarriaga 1997; Hu & White 1997; Kamionkowski & Kosowsky 1998). While the amplitude of the *B*-mode signal is unknown, the shape of the spectrum is robustly predicted by theory. The primordial *B*-mode power spectrum has a characteristic double-humped shape, the first bump on large angular angular scales ( $\ell < 10$ ) produced at reionization epoch and the second on degree scales produced during electron-photon decoupling around the time of recombination. The *B*-mode power at degree angular scales is related to the amount of primordial gravitational waves emitted during inflation, and is quantified by the tensor-to-scalar ratio  $r$ . The amplitude of this background is determined by the energy scale of inflation (Knox & Turner 1993), which can widely vary among different inflationary models. CMB *B*-mode polarization hence give us a mean to investigate the physics of the inflation. This makes the search for the *B*-mode polarization crucially linked to a probe of the inflationary scenario.

*Planck* is considered the definitive mission about CMB temperature anisotropies at angular scales larger than 5 arcmin. However, the sensitivity of *Planck* was insufficient to extract all the information carried by CMB polarization. For a definitive measurement, the sensitivity to polarization signals needs to be improved at least by one or two orders of magnitude.

CMB polarization *B*-modes are known to be much fainter than CMB temperature anisotropies and polarization *E*-modes. Hence, their detection constitutes a major technological challenge. However, recent developments in detector technology have made this exciting prospect possible. Although the signal still remains elusive, the latest observations of the sky by the Planck satellite has put an upper limit on the tensor-to-scalar ratio  $r_{0.05} < 0.056$  at 95% confidence level. This upper limit is further tightened by combining with the BICEP2/Keck Array BK18 data to obtain  $r_{0.05} < 0.036$  (Ade et al. 2021). The upper bound on  $r$  combined with the the measurement of the primordial spectral index  $n_s$  have been able to rule out a large number of inflationary models. The simplest slow-roll models that naturally explain the observed departure of  $n_s$  from unity predict  $r > 0.001$ . The inflation models such as Starobinsky  $R^2$ ,  $\alpha$ -attractor and D-brane inflation are strongly favored while some class of models such as natural inflation, low-scale SUSY (supersymmetry) have been ruled out with significance of more than  $2\sigma$  level (Akrami et al. 2020). A detection of the *B*-modes or even achieving a tighter upper bound of  $r \sim 10^{-3}$  will give us a deeper understanding of the infla-

tionary physics and its energy scale that would shed light on the mechanism that created the primordial perturbations.

The importance of this scientific goal has triggered the scientific community to build highly sensitive instruments and plan for new ground-based and space-based projects. Among the experiments that are currently ongoing or in preparation, ground based experiments are expected to be limited by their restricted frequency and sky coverage, while the LiteBIRD (Hazumi et al. 2019) space mission, owing to its limited angular resolution ( $\sim 30'$ ), will be limited by confusion between primordial and lensing polarization *B*-modes. To overcome these limitations, other experiments have been proposed, such as COrE (The COrE Collaboration et al. 2011; Delabrouille et al. 2018), PRISM (André et al. 2014), PICO (Hanany et al. 2019), and more recently an ambitious spectro-polarimetric survey of the microwave sky (Delabrouille et al. 2019). Exploring Cosmic History and Origin (ECHO)<sup>1</sup> is the latest addition to this list with similar objectives.

ECHO is a proposal for a next generation space mission for near-ultimate measurements of the CMB polarization and discovery of global CMB spectral distortions. The proposal is primarily inspired from the concept of the COrE mission and borrows many of its most appealing design aspects (Delabrouille et al. 2018; de Bernardis et al. 2018), and it is under consideration to the Indian Space Research Organization (ISRO)<sup>2</sup>. The objective of this paper is to forecast the potential of this mission to achieve the main goal, the measurement of tensor-to-scalar ratio. Similar forecasting constraints on  $r$  have been done for many proposed or ongoing CMB missions (Remazeilles et al. 2016; Errard et al. 2016; Alonso et al. 2017; Remazeilles et al. 2018; Hanany et al. 2019; Abazajian et al. 2022).

The paper is arranged as follows. Section 2 describes in detail the objective of ECHO space mission: foreground cleaning challenge and the specification of the instrument. This is followed by a discussion of the simulation of the microwave sky for different foreground models and component separation methods used for the analysis in Section 3 and Section 4 respectively. The main results of the analysis are summarized in Section 5. Finally, we conclude in Section 6.

## 2 ECHO

### 2.1 Sensitivity objectives and requirements

ECHO aims to detect and characterize the primordial gravitational waves by measuring *B*-modes of CMB polarization signal at large angular scales. A quantitative goal for the full success of ECHO is to achieve a 68% confidence level on measurement of the tensor-to-scalar ratio of the order of  $10^{-3}$ . Achieving this science goal requires:

- Low detector noise and measurement errors: State of the art detectors built using current technology are limited by the fundamental photon noise, and so the sensitivity of individual detectors cannot be improved much. Hence, the only way to improve the sensitivity of the instruments, is to build

<sup>1</sup> <https://cmb-bharat.in/>

<sup>2</sup> <https://www.isro.gov.in/>

large focal plane instruments with thousands of detectors, which, in effect, make many simultaneous measurements. In addition to these detectors, one must cope with the thermal emission of the telescope and the endowment around it. This limits our choice to place the instruments because only space instruments are expected to be cold enough to avoid such local emission. A very subtle shift or rotation of a detector, or glint of light from out of the field could mimic a spurious signal. The design of the instruments, the program of mapping and observation, the experimental characterization and calibration of the experiment will all need to be carried out with an unparalleled level of precision so that the instrumental systematic effects must be controlled to level well below the sensitivity of the instrument.

- **Removal of foreground contamination:** The capability to distinguish CMB  $B$ -mode polarization from contamination by galactic and extragalactic astrophysical emissions is determined by multitude of astrophysical signals, frequency range and number of bands the mission has across the microwave and sub-millimeter range. The foreground and cosmological signals are separable using their spectral signatures. Although CMB is same at all frequency bands (in thermodynamic unit), the electromagnetic spectrum of the astrophysical components are different across frequencies. The CMB  $B$ -mode signal is expected to be very weak and buried in the astrophysical foregrounds (we discuss this issue in more detail in Section 2.2). Thus, to characterize astrophysical foreground emission and efficiently subtract them from CMB, we need large frequency coverage.

- **Removal of contamination due to lensing:** At large angular scales ( $\ell < 150$ ), the  $B$ -modes transformed from  $E$ -modes due to gravitational lensing resemble as white noise of approximately constant amplitude of  $5 \mu\text{K}\cdot\text{arcmin}$  (Seljak & Hirata 2004). The lensing  $B$ -modes and primordial  $B$ -modes are comparable at  $\ell = 80$  for tensor-to-scalar ratio  $r \approx 0.01$ . The lensing  $B$ -modes has dominant contribution to uncertainties of  $r$  measurement if noise level is lower than the lensing signal of  $5 \mu\text{K}\cdot\text{arcmin}$ . Therefore, to reach the target level of tensor-to-scalar ratio of the order of  $10^{-3}$ , lensing correction is necessary. This requires an angular resolution of a few arcmin at observation frequencies in the 100 – 200 GHz range (and below if possible).

To take these requirements into account, the ECHO satellite will scan the microwave sky in temperature and polarization in 20 frequency bands ranging from few tens of GHz to THz. The satellite will be placed in orbit around Sun-Earth second Lagrange (L2) point. The observations will be carried out for 4 years in the anti-solar direction, pointing away from contaminating radiation from the Sun, the Earth and the Moon. The instrument will measure the CMB polarization field down to angular scales of a few arcminutes with a sensitivity of 1-2  $\mu\text{K}\cdot\text{arcmin}$ .

Table 1 presents the instrument specification of ECHO. ECHO is inspired by the COreE concept and borrows many of its most appealing design aspects (Delabrouille et al. 2018; de Bernardis et al. 2018). It improves the COreE concept by extending the frequency coverage at both high and low end of frequency coverage while also enhancing the sensitivity roughly by a factor of  $\sqrt{2}$ . ECHO scanning strategy will cover the full sky with multiple visits to the same sky location over a period of 4 years of observations. Fig. 1 compares the

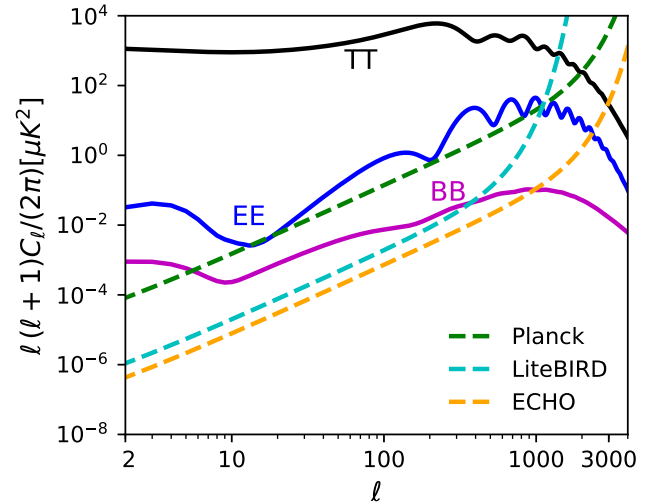


**Figure 1.** Theoretical CMB angular power spectra of temperature  $T$ ,  $E$ - and  $B$ -mode polarization anisotropies as a function of multipole moments for the best-fit  $\Lambda\text{CDM}$  parameters derived by *Planck* (Planck Collaboration VI 2018) with  $r = 0.06$ . The instrument noise power spectrum of polarization (dash lines) plotted for different generations of space based CMB surveys, viz. *Planck*, *LiteBIRD* and *ECHO*.

target ECHO noise power spectra polarization with those of different generations of space based CMB surveys (existing or planned).

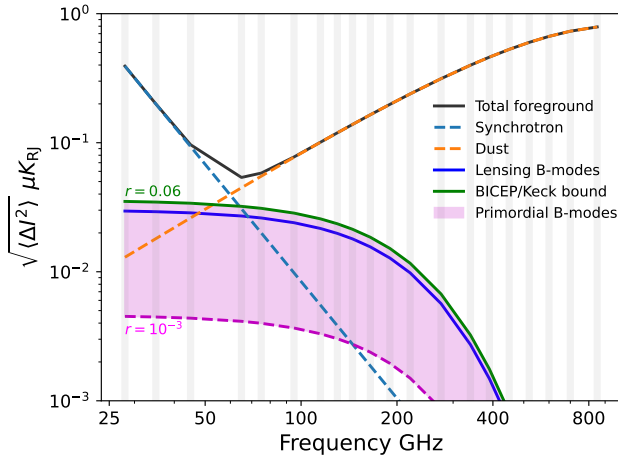
ECHO is designed to allow for maximum control over foregrounds. Fig. 2 shows that three ECHO channels below 50 GHz are dominated by synchrotron emission while the 14 channels above 100 GHz are dominated by dust emission. The high frequency channels of the instrument, particularly the frequency channels from 220 to 900 GHz, are designed to remove the dust contamination in CMB and measure the Cosmic Infrared Background (CIB) anisotropies. On the other hand the low frequency channels are designed to mitigate the contamination of CMB polarization measurements by Galactic synchrotron emission. The channels between 50 and 200 GHz can be thought of as the CMB channels, that are expected to drive the detection of the primordial  $B$ -mode signal. In essence, ECHO configuration aims to observe the polarized microwave sky with 10 – 30 times better sensitivity than *Planck* and will more than double the frequency coverage.

## 2.2 The foreground issue

The weakness of the CMB polarization signal makes it heavily contaminated by foreground emission from both the galactic and extragalactic sources. The extragalactic foregrounds such as point sources are approximately white noise, whereas the galactic synchrotron and dust emission are expected to have a significant polarization at large angular scales. The minimum polarized foreground contamination is roughly corresponding to  $r_{\text{FG}} = 0.06$  to 1.0 in the frequency range 60–100 GHz (Krachmalnicoff, N. et al. 2016). In fact, depending on the amplitude of  $r$  and scaling of foreground components, the signal could be buried nearly two orders of magnitude below the foreground contamination as shown

**Table 1.** ECHO instrument specification as proposed in the CMB-Bhārat proposal.

Frequency (GHz)	Beam FWHM (arcmin)	$Q$ & $U$ noise r.m.s ( $\mu\text{K}\cdot\text{arcmin}$ )
28	39.9	16.5
35	31.9	13.3
45	24.8	11.9
65	17.1	8.9
75	14.91	5.1
95	11.7	4.6
115	9.72	3.1
130	8.59	3.1
145	7.70	2.4
165	6.77	2.5
190	5.88	2.8
220	5.08	3.3
275	4.06	6.3
340	3.28	11.4
390	2.86	21.9
450	2.48	43.4
520	2.14	102.0
600	1.86	288.0
700	1.59	1122.0
850	1.31	9550.0

**Figure 2.** This figure depicts the root mean square (r.m.s) fluctuations associated with the synchrotron, dust and the CMB  $B$ -mode signal. The solid black line represents the total foreground. The magenta band denotes the CMB for the range of  $r \in [0.001, 0.06]$ . The vertical gray bands mark the ECHO channels.

in Fig. 2. Given the current upper limits on  $r$ , there is no regions of the sky which are dominated by the primordial  $B$ -mode signal. Therefore a robust measurement of primordial  $B$ -modes will require foreground removal to anticipated levels. In order to achieve the target of ECHO, residual in the recovered CMB maps should be controlled below  $10^{-5}\mu\text{K}^2$ .

Unlike the intensity foregrounds, the polarized foreground sky is relatively less complex and, dominated primarily by synchrotron and dust emissions. The diffuse synchrotron emission is generated from gyrating relativistic cosmic ray leptons in the galactic magnetic field. It is modeled by the density of cosmic ray leptons, their spectral properties, the galactic magnetic field (Fauvet, L. et al. 2011;

Orlando & Strong 2013). The thermal dust emissions from elongated grains aligned in galactic magnetic field (Lazarian 2007) is the dominant galactic emission at frequencies greater than 100 GHz. The emission law of the thermal dust can be fitted with a modified black-body (MBB) (Planck Collaboration X 2016). In addition to these two main astrophysical emissions, anomalous microwave emission (AME) from spinning dust grains with low polarization fraction, may be a relevant component at 10 – 60 GHz (Leitch et al. 1997; de Oliveira-Costa et al. 2004; Finkbeiner 2004). Extragalactic objects also emit polarized light that have varied spectral energy distribution and polarization properties (Saikia & Salter 1988) having a median polarization of 2% (Bonavera et al. 2017; Trombetti et al. 2018; Puglisi et al. 2018). However, the impact of these sources is relatively small at large angular scales.

In recent years, quite a large number of component separation methods have been developed. Some of them are already implemented on high quality cosmological data sets such as *Planck*. While these methods primarily aim at cleaning CMB maps, they differ from each other in their domain of implementation. While the primary goal of ECHO is to study the CMB polarization maps, a great interest lies in a deeper understanding of the polarization properties of astrophysical emission processes too. Hence, we approach the CMB cleaning in two different ways: treating CMB as one of the many physical signal we want to recover together with synchrotron and thermal dust emissions, or focusing on isolating the CMB regardless of the physical mechanisms responsible for the contaminating emissions.

The component separation pipelines considered in this work are the *Commander* (Eriksen et al. 2004, 2008) and the Needlet Internal Linear Combination (NILC, Delabrouille et al. 2009; Basak & Delabrouille 2012, 2013). In the *Commander* pipeline, the foreground parameters are fitted through Bayesian parameter estimation technique operating on real (pixel) space. NILC is an implementation of Internal Linear Combination (ILC, Tegmark & Efstathiou 1996) of the frequency channels under consideration with minimum error variance, on a frame of spherical wavelets called needlets (Narcowich et al. 2006). This method allows localized filtering in both pixel space and harmonic space. This particular implementation of ILC has the advantage that the weights used to combine the sky can vary with a position on the sky and also with an angular scale.

For  $r \sim 10^{-3}$ , the cosmic variance errors associated with lensing  $B$ -modes will limit the statistical significance with which primordial  $B$ -mode signal can be measured. Therefore, to improve the sensitivity of  $r$  measurement, the lensing contribution must be reduced exploiting the delensing techniques with the aid of CMB lensing map, CIB map, external galaxy survey data sets (Sherwin & Schmittfull 2015; Manzotti et al. 2017; Manzotti 2018; Baleato Lizancos et al. 2021). ECHO is design to provide high resolution  $E$ -mode and CIB maps after applying the component separation techniques to the total frequency maps which will help in lensing correction.



### 3 SKY MODELING

In this section, we describe the models of each of the sky components (CMB, thermal dust, synchrotron, AME and point sources) used in our analysis.

Since the prime focus of this work is to study the  $B$ -modes of CMB polarization at large angular scales, we consider only the polarized emission of the foregrounds and do not include the secondary anisotropies such as Sunyaev-Zel'dovich effect, patchy reionization effect (Smith & Ferraro 2017; Mukherjee et al. 2019) and any extragalactic diffuse emission e.g. CIB in our analysis. We integrate over top-hat bandpass profile around central frequencies in simulating the maps.

#### 3.1 CMB

We use *Planck* 2018 best-fit  $\Lambda$ CDM model (Planck Collaboration VI 2018) for tensor-to-scalar ratio  $r = 0$  to model the CMB sky. The theoretical angular spectra of CMB and lensing potential are obtained using CAMB<sup>3</sup>. The lensed CMB maps are generated from the theory spectra using the LensPix<sup>4</sup> package. For CoRE mission, it has been investigated that reduction of the lensing  $B$ -mode power is possible by 70 % using CMB lensing and CIB maps (Remazeilles et al. 2018). Since ECHO instrument design is motivated by CoRE concept, we are optimistic to achieve similar or plausibly better delensing in future. Therefore, in addition to fully lensed CMB maps, we also consider 84 % delensed CMB maps in our work. These maps are generated from the weighted linear combination of the unlensed and lensed CMB maps as

$$\text{Total CMB} = \sqrt{A_L} \times \text{lensed CMB} + (1 - \sqrt{A_L}) \times \text{unlensed CMB}, \quad (1)$$

where  $A_L$  is the lensing amplitude.  $A_L = 1$  for no delensing case and  $A_L = 0.16$  for 84% delensing case.

#### 3.2 Thermal dust model

In this forecast study, we use three dust polarization templates with different complexities.

- **GNILC – dust:** In this model, we first generate the dust intensity maps  $I_v^{\text{GNILC}}$  (Planck Collaboration XLVIII 2016) at ECHO frequencies assuming a single component MBB spectrum,

$$I_v^{\text{GNILC}} = \tau_{353} \left( \frac{\nu}{353} \right)^{\beta_d} B_\nu(T_d) \quad (2)$$

where  $\tau_{353}$  is the dust optical depth normalized at 353 GHz,  $\beta_d$  is the dust spectral index,  $T_d$  is the dust temperature, and  $B_\nu$  is the planck function. The full-sky maps of  $\tau_{353}$ ,  $\beta_d$  and  $T_d$  are obtained by fitting the MBB spectrum to the CIB-subtracted *Planck* 353, 545, and 857 GHz intensity maps and IRIS 100  $\mu\text{m}$  map. The CIB anisotropies are disentangled from the total intensity maps using the Generalized Needlet Internal Linear Combination (GNILC) pipeline (Remazeilles et al. 2011).

<sup>3</sup> <https://camb.info/>

<sup>4</sup> <http://cosmologist.info/lenspix/>

These intensities are converted into the Stokes  $Q$  and  $U$  parameters as follows,

$$\begin{aligned} Q_v^d &= u_v f_d g_d I_v^{\text{GNILC}} \cos(2\gamma_d) \\ U_v^d &= u_v f_d g_d I_v^{\text{GNILC}} \sin(2\gamma_d), \end{aligned} \quad (3)$$

where  $\gamma_d$  is the dust polarization angle arises due to the Galactic magnetic field configuration (Miville-Deschênes et al. 2008),  $f_d$  is the dust polarization fraction and  $g_d$  is the depolarization factor. The polarization angle map ( $\gamma_d$ ) and  $g_d$  at scales greater than  $20^\circ$  are derived from the large-scale model of the Galactic magnetic field (Miville-Deschênes et al. 2008; O’Dea et al. 2011). It is then combined with synchrotron polarization angle ( $\gamma_s$ ) and depolarization factor ( $g_s$ ) maps estimated from the 23 GHz WMAP polarization data and 408 MHz (Haslam et al. 1982) templates to add the structures at intermediate scales between  $3^\circ$  and  $20^\circ$ . The small-scale ( $< 3^\circ$ ) features of  $\gamma_d$  and  $g_d$  are added using the method described in Miville-Deschênes, M.-A. et al. (2007). The combination of different scales to produce high resolution map of  $\gamma_d$  is discussed in Delabrouille, J. et al. (2013). We set  $f_d = 0.15$ , which gets reduced to observed polarization fraction  $f_d g_d = 0.05$  on average over the sky. The unit conversion factor ( $u_v$ ) takes into account the conversion from MJy/sr to  $\mu\text{K}_{\text{CMB}}$  units (or thermodynamic temperature units).

- **TD – dust:** Ghosh et al. (2017) and Adak et al. (2020) build a dust polarization model at 353 GHz at high Galactic latitude using three phases of HI clouds, cold, warm and unstable neutral medium of ISM and phenomenological magnetic field (Planck Collaboration XLIV 2016). This model can describe the dust properties within the scale,  $40 < \ell < 160$ . We scale those templates at other frequencies with a MBB spectrum using spatially varying  $T_d$  of  $19.4 \pm 1.4$  K and  $\beta_d$  with a value of  $1.53 \pm 0.02$  (Planck Collaboration XI 2020; Planck Collaboration 2014). The  $\beta_d$  and  $T_d$  maps for each HI phase are generated from a Gaussian distribution mean and standard deviation stated above. We do not introduce any correlation between  $\beta_d$  and  $T_d$  maps for each HI phase across the sky. We treat the three HI phases as emitting layers with the same spectral properties/different spectral properties to generate polarized dust maps without/with frequency decorrelation<sup>5</sup>. We introduce 0.2 % decorrelation at  $\ell = 80$  between 217 and 353 GHz over 24 % of the unmasked sky. We choose this model in order to specifically assess the performance of foreground subtraction with the Commander pipeline in the presence of dust decorrelation across the frequencies.

- **MKD – dust:** We make use of the multi-layer dust model of Martínez-Solaesche et al. (2018) based on the dust extinction maps from Green et al. (2015), and generate model Stokes  $Q$ ,  $U$  parameters with different emission laws in six different layers in their modeling framework. By construction, this

<sup>5</sup> Since intrinsic local polarization fraction,  $p(r)$ , optical depth,  $\tau(r)$ ,  $T_d$ ,  $\beta_d$ ,  $\gamma_d$ , all these parameters change along line-of-sight (LOS), the polarization angle and polarization fraction in each emitting layers are different and function of frequencies. This rotation of the polarization angle along LOS will automatically introduce the depolarization effect (Pelgrims, V. et al. 2021). However, use of different spectral maps at different layers in this case does not guarantee that the amount of decorrelation will be the same as observed in Planck Collaboration XI (2020).

model generates decorrelation between the frequency channels. The amount of decorrelation present in the model is 0.5 % at  $\ell = 80$  between 217 and 353 GHz over 70 % of the unmasked sky.

### 3.3 Synchrotron model

We consider following three different emission law models of galactic synchrotron emission. For all the models, we use the synchrotron  $Q$ ,  $U$  maps obtained from Spectral Matching Independent Component Analysis (SMICA) at the reference frequency  $\nu_0 = 30$  GHz as the template maps (Planck Collaboration IV 2018).

- **Power – law:** In this model, the synchrotron  $Q_\nu^s$  and  $U_\nu^s$  maps at any frequency  $\nu$  are generated by scaling the synchrotron template Stokes  $Q_{\nu_0}^s$  and  $U_{\nu_0}^s$  maps (expressed in MJy/sr units) at the reference frequency  $\nu_0$  using a power-law model,

$$\begin{aligned} Q_\nu^s &= u_\nu Q_{\nu_0}^s \left(\frac{\nu}{\nu_0}\right)^{\beta_s+2} \\ U_\nu^s &= u_\nu U_{\nu_0}^s \left(\frac{\nu}{\nu_0}\right)^{\beta_s+2}, \end{aligned} \quad (4)$$

where  $\beta_s$  is the spatially varying synchrotron spectral index map. It is derived by fitting 408 MHz and WMAP 23 GHz polarization data using model 4 of [Miville-Deschênes et al. \(2008\)](#). The average value of  $\beta_s$  is  $-3.0$  over the whole sky. The  $u_\nu$  denotes the unit conversion factor from MJy/sr to  $\mu K_{\text{CMB}}$  units.

- **Curved – power – law:** In this model, the synchrotron template maps are scaled to other frequencies using the spectral index,

$$\beta_s = -3.11 + C \log\left(\frac{\nu}{23}\right). \quad (5)$$

We adopt  $C = -0.3$  for frequencies larger than 23 GHz, which accounts for the steepening of the synchrotron spectrum ([Kogut et al. 2007](#)).

- **GALPROP:** In this model, the synchrotron template maps are translated to other frequencies using a fixed GALPROP scaling parameter  $\alpha = 0.26$  (Planck Collaboration X 2016). The synchrotron emission spectrum for  $\alpha = 0.26$  is simulated from GALPROP<sup>6,7</sup> code of [Orlando & Strong \(2013\)](#).

### 3.4 AME model

We model the AME  $Q$  and  $U$  maps as

$$\begin{aligned} Q_\nu^{\text{AME}} &= p_{\text{AME}} I_\nu^{\text{AME}} \cos(2\gamma_d) \\ U_\nu^{\text{AME}} &= p_{\text{AME}} I_\nu^{\text{AME}} \sin(2\gamma_d), \end{aligned} \quad (6)$$

where the AME intensity,  $I_\nu^{\text{AME}}$  at the reference frequency 23 GHz is derived from GNILC thermal dust intensity at 353 GHz rescaled by a factor of 0.91 K/K (Planck Collaboration XXV 2016).  $I_\nu^{\text{AME}}$  follows a cold neutral medium model emission law as derived in [Ali-Haïmoud et al. \(2009\)](#) that has been used to extrapolate 23 GHz AME template to

ECHO frequencies. We assign to AME emission a constant polarization fraction of  $p_{\text{AME}} = 1\%$ , compatible with observational upper limits ([Dickinson et al. 2011](#); [Génova-Santos et al. 2015](#)). We assume polarization angle  $\gamma_d$  to be same as those for thermal dust since both components are correlated.

### 3.5 Point source model

We consider faint radio and infrared extragalactic sources. The radio sources are taken from radio surveys of PMN/GB6, NVSS, SUMSS at 4.85, 1.4, and 0.843 GHz ([Delabrouille, J. et al. 2013](#)). Then the fluxes of the sources are extrapolated to ECHO frequencies using power-law,  $S_\nu \propto \nu^{-\alpha}$ . Depending on the spectral index, the sources are divided into two categories (the boundary value being  $\alpha = 0.5$ ); steep- and flat-spectrum class. The polarization fraction is randomly assigned with mean values of 2.7% and 4.8% for flat- and steep classes, respectively, consistent with the results of [Ricci, R. et al. \(2004\)](#). The faint sources are separated from strong sources following PCCS2 detection limits at 30, 70, 353, 857 GHz giving the flux limit of 0.427, 0.501, 0.304, 0.791 Jy (Planck Collaboration et al. 2016).

We consider the Infrared Astronomical Satellite (IRAS) faint point sources catalogue ([Moshir et al. 1992](#)) and extrapolated them to ECHO frequencies with modified blackbody spectra,  $\nu^b B(\nu, T)$  with  $b = 1.3$  and  $T = 35$  K ([Dunne et al. 2000](#); [Delabrouille, J. et al. 2013](#)). The polarization fraction is assigned randomly drawn from the  $\chi^2$  distribution of one degree of freedom with a mean polarization fraction of 1.5 %, and the polarization angle is drawn from a uniform distribution.

### 3.6 Sky simulations

We use the recent version of the Planck Sky Model<sup>8</sup> (PSM v2.0.2, [Delabrouille, J. et al. 2013](#)) to simulate full-sky maps for most of the sky configurations. In addition, we use the polarized dust templates of Stokes  $Q$  and  $U$  maps from MKD – dust ([Martínez-Solaesche et al. 2018](#)) and TD – dust ([Ghosh et al. 2017](#); [Adak et al. 2020](#)) models as described in Section 3.2. Table 2 summarizes all the sky components and their models included in the simulations. To test the efficiency of the two component separation methods in the recovery of  $r$ , we choose to work with low HEALPIX pixel resolution of  $N_{\text{side}} = 512$  for NILC and  $N_{\text{side}} = 256$  for Commander. We first simulate all the component maps (CMB, foreground and instrumental noise) at  $N_{\text{side}} = 512$ . For consistency with our choice of  $N_{\text{side}}$ , CMB and foreground maps at  $N_{\text{side}} = 512$  are smoothed at the respective beam resolution specified in Table 1 for the frequency channels below 65 GHz and a FWHM = 20' for rest of the frequency channels. These maps are used for NILC analysis. For Commander, we apply additional smoothing to make all the maps at a common beam resolution of 60' FWHM and downgraded to  $N_{\text{side}} = 256$ .

In Table 3, we summarize the set of sky configurations together with the different choices of foreground cleaning algorithms employed. We include the polarized thermal dust and synchrotron emissions to all the set of simulations that correspond to a different models of dust and synchrotron

<sup>6</sup> <https://galprop.stanford.edu/>

<sup>7</sup> <https://sourceforge.net/projects/galprop/>

<sup>8</sup> <http://www.apc.univ-paris7.fr/delabrou/PSM/psm.html>

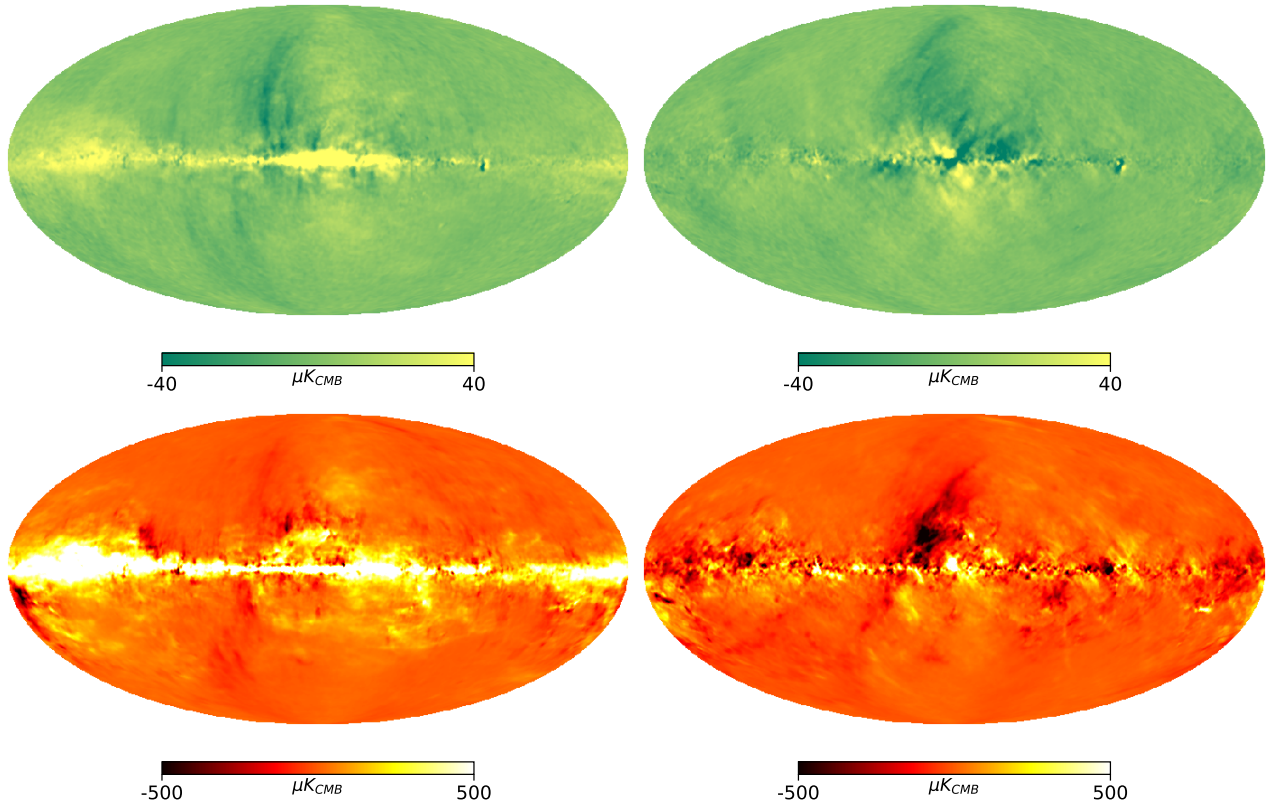


**Figure 3.** Simulated Stokes  $Q$  and  $U$  maps for SET1a at synchrotron dominated 35 GHz channel (*upper panel*) and thermal dust dominated 340 GHz channel (*lower panel*).

emission. For SET3a-b sky configurations, we choose to work with  $N_{\text{side}} = 128$  maps with 60' FWHM beam smoothing. Since the TD – dust templates are produced at  $N_{\text{side}} = 128$ , the other foreground components are further downgraded to  $N_{\text{side}} = 128$  to match the HEALPix pixelization scheme.

We generate the two half-mission (HM1 & HM2) and one full-mission Gaussian white noise realizations at each frequency. For simulating the half-mission noise, we use the  $\sqrt{2}$  times the r.m.s noise level listed in Table 1. Noise maps are smoothed to final beam FWHM for each channel. Finally, we coadd CMB, foreground and noise realization maps at each frequency to produce the two half-mission data sets of the observed sky at respective ECHO frequencies. The final sky maps are expressed in thermodynamic unit. Figure 3 presents the full-sky Stokes  $Q$  and  $U$  maps at 35 GHz (*upper panel*; synchrotron dominated channel) and 340 GHz (*lower panel*; thermal dust dominated channel) for the sky configuration SET1a.

## 4 METHODS

### 4.1 Component separation pipelines

In this section, we briefly describe the two component separation methods (**Commander** and NILC) that have been implemented to recover the  $B$ -mode of CMB from multi-frequency simulations of the sky. As far as the implementation of these methods is concerned, these two methods differ a lot from each other, but, they are complementary to each other.

While NILC exploits the black body frequency scaling of the CMB and minimizes the variance of the linear mixture of the sky operating on spherical wavelet domain with minimum assumption of the foreground emissions, the **Commander** makes use of the prior knowledge of the foreground emissions characterized by the parameters which are fitted using Bayesian techniques operating on pixel domain.

#### 4.1.1 Commander Implementation

**Commander** assumes that the observed sky can be described using parametric model and is a linear superposition of the foreground emissions and instrumental noise superimposed on true CMB. The central idea behind this method is the use of Gibbs sampling technique (Wandelt et al. 2004) to sample from joint posterior distribution by cycling through conditional distributions (Eriksen et al. 2004, 2008). We use the publicly available version of **Commander** code, called **Commander1**<sup>9</sup>. We fit the HM1 and HM2 simulations at each pixel  $p$  with the model consisting of CMB, dust and synchrotron emissions. The foregrounds (dust and synchrotron) spectra are modelled in terms of few free parameters characterizing their amplitudes and spectral indices,

$$d_{\nu}(p) = s^{cmb}(p) + \sum_{i=1}^{N_{\text{foreground}}} F_{\nu}^i(\beta_i(p)) f^i(p) + n_{\nu}(p), \quad (7)$$

<sup>9</sup> <https://github.com/Cosmoglobe/Commander>

**Table 2.** Summary of the sky components and their parametric model used in simulations.

Component	Emission law	Nomenclature	Additional information/Templates
CMB	Blackbody with scaling, $a_\nu = \frac{dB_\nu(T)}{dT} _{T_{CMB}}$ ; $T_{CMB} = 2.725\text{K}$		$r = 0$
Thermal dust	MBB	GNILC – dust	<i>Planck</i> GNILC maps at 353 GHz from <a href="#">Planck Collaboration XLVIII (2016)</a>
		TD – dust	Hi based dust polarization model at high galactic latitude developed in <a href="#">Ghosh et al. (2017)</a> and <a href="#">Adak et al. (2020)</a> at 353 GHz
		MKD – dust	Multi-layer dust model based on dust extinction maps developed in <a href="#">Martínez-Solaache et al. (2018)</a>
Synchrotron	Power-law, spatially varying spectral index with $\langle\beta_s\rangle = -3$	Power – law	SMICA $Q, U$ maps from <a href="#">Planck Collaboration IV (2018)</a> at 30 GHz
		Curved–power–law	SMICA $Q, U$ maps from <a href="#">Planck Collaboration IV (2018)</a> at 30 GHz
		GALPROP	SMICA $Q, U$ maps from <a href="#">Planck Collaboration IV (2018)</a> at 30 GHz
Spinning dust	CNM emission law with 1 % polarization fraction and dust polarization angle		<i>Planck</i> thermal dust intensity at 353 GHz ( <a href="#">Planck Collaboration XLVIII 2016</a> ) scaled at 23 GHz with correlation coefficient of 0.91 K/K
			Radio sources have median polarization fraction of 2.7 % and 4.8 % for two class of power-laws;
Point-sources	Sources from radio surveys extrapolated with power laws;		
	IRAS survey modelled with modified blackbody emission laws.		IR sources are taken from IRIS data and having mean polarization fraction of 1.5 %

**Table 3.** Set of simulations and pipelines used in the analysis. The tick and cross symbols indicate which components are added and excluded respectively for different configurations. The dust and synchrotron models used can be identified using nomenclatures listed in [Table 2](#).

Sim.ID	Pipeline		Dust	Synchrotron	AME	point-sources	delensing	Decorrelation
	Commander	NILC						
SET1a	✓	✓	GNILC – dust	GALPROP	✗	✗	✗	✗
SET1b	✓	✓	GNILC – dust	GALPROP	✓	✗	✗	✗
SET1c	✓	✓	GNILC – dust	GALPROP	✓	✓	✗	✗
SET1d	✓	✓	GNILC – dust	GALPROP	✗	✗	✓	✗
SET1e	✓	✓	GNILC – dust	Power – law	✓	✓	✗	✗
SET1f	✓	✓	GNILC – dust	Curved–power–law	✓	✓	✗	✗
SET2a	✓	✓	MKD – dust	GALPROP	✓	✓	✗	✓
SET2b	✓	✓	MKD – dust	Power – law	✓	✓	✗	✓
SET2c	✓	✓	MKD – dust	Curved–power–law	✓	✓	✗	✓
SET3a	✓	✗	TD – dust	GALPROP	✓	✓	✗	✗
SET3b	✓	✗	TD – dust	GALPROP	✓	✓	✗	✓



where  $s^{cmb}$  and  $f^i$  are the CMB and foreground amplitudes respectively at some reference frequency. In thermodynamic units, the CMB amplitude is constant across the frequencies. We choose 28 GHz and 340 GHz as the reference frequency for synchrotron and dust respectively. The frequency scaling coefficients  $F_\nu^i(\beta_i(p))$  are set by the parametric model of the spectral emission laws of the foregrounds, and  $n_i$  is the instrumental noise. We fit the MBB spectrum of the dust and different emission law models (power-law, curved power-law, and GALPROP) for the synchrotron to each of the half-mission data sets. We use Gaussian priors for dust temperature,  $T_d = 19 \pm 0.3$  K, dust spectral index,  $\beta_d = 1.6 \pm 0.3$  and synchrotron spectral index,  $\beta_s = -3.0 \pm 0.2$  along with Jeffreys priors (Jeffreys 1939).

The detailed sampling method has been described in Eriksen et al. (2008). The method is computationally demanding, and hence can work only with the low-resolution HEALPix maps at  $N_{\text{side}} = 256$  and 128. We draw the samples of the parameters over the full-sky for all the sky configurations, except SET3a and SET3b.

For SET1a-d, the data model we fit within the Commander framework is the same as the one used for the sky simulations. However, for SET2a-c and SET3a-b, there is a mismatch between the simulated maps and the data model due to the presence of the dust decorrelation. This model mismatch could result into a excess bias on the estimation of  $r$ . In principle, we could reduce this bias by fitting the dust decorrelation parameters in the Commander framework. As our polarized dust simulations capture the sky complexity, it is not simple to find a parametric model that captures the dust decorrelation fully.

#### 4.1.2 NILC Implementation

On contrary to Commander method, NILC is a blind component separation method. It is implementation of ILC of the frequency channels with minimum error variance, on a frame of spherical wavelets called needlets, allowing localized filtering in both pixel domain and harmonic domain.

The NILC pipeline (Delabrouille et al. 2009; Basak & Delabrouille 2012, 2013) is designed to be applicable to scalar fields on sphere. Therefore, we work separately on  $E$  and  $B$  maps decomposed from  $Q$  and  $U$  maps. Prior to the implementation of the NILC to the simulated maps, polarization maps of the sky at each frequency are de-convolved to a common beam resolution which is Gaussian beam of FWHM =  $20'$  in our case. The common resolution sky maps are then decomposed into a set of needlet coefficients for different needlet scales. The needlet coefficients at different needlet scale  $j$  are obtained using needlet filters  $h_\ell^j$  designed as follows:

$$h_\ell^j = \begin{cases} \cos\left[\left(\frac{\ell^j_{\text{peak}} - \ell}{\ell^j_{\text{peak}} - \ell^j_{\text{min}}}\right)\frac{\pi}{2}\right] & \text{for } \ell^j_{\text{min}} \leq \ell < \ell^j_{\text{peak}} \\ 1 & \text{for } \ell = \ell^j_{\text{peak}} \\ \cos\left[\left(\frac{\ell - \ell^j_{\text{peak}}}{\ell^j_{\text{max}} - \ell^j_{\text{peak}}}\right)\frac{\pi}{2}\right] & \text{for } \ell^j_{\text{peak}} < \ell \leq \ell^j_{\text{max}}. \end{cases} \quad (8)$$

For each scale  $j$ , the filter has a compact support between ranging between the multipoles  $\ell^j_{\text{min}}$  and  $\ell^j_{\text{max}}$  with a

**Table 4.** List of needlet bands used in the analysis.

Band index	$\ell_{\text{min}}$	$\ell_{\text{peak}}$	$\ell_{\text{max}}$	$N_{\text{side}}$
1	0	0	50	32
2	0	50	100	64
3	50	100	200	128
4	100	200	300	128
5	200	300	400	256
6	300	400	500	512
7	400	500	600	512
8	500	600	700	512
9	600	700	800	512
10	700	800	900	512
11	800	900	1000	512

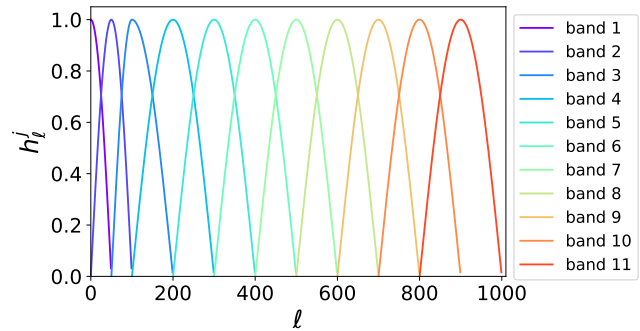


**Figure 4.** The needlet filter function  $h_\ell^j$  for eleven needlet bands.

peak at  $\ell^j_{\text{peak}}$ . For our purpose, we have used 11 needlet bands listed in Table 4 and corresponding filters are shown in Fig. 4. The needlet coefficients are computed at HEALPix grid points with a resolution,  $N_{\text{side}}$  equal to the smallest power of 2 larger than  $\ell^j_{\text{max}}/2$ . The corresponding  $N_{\text{side}}$  for different needlet scales are listed in Table 4.

For each scale, the NILC weights are determined by minimizing the variance of the linear combination of the sky in such a way that the foreground and noise component present in sky is minimized while the CMB component remain unaffected. Finally, the CMB is extracted by linearly combining the sky at each frequency through the NILC weights. Thus, the contribution of each frequency channel towards the reconstructed CMB map can be easily demonstrated through the NILC weights.

#### 4.2 Galactic masks

To minimize the impact of foreground residuals on the measurement of  $r$ , we apply a conservative mask. We put thresholds on the synchrotron and dust polarization intensity maps to prepare the confidence mask for Commander (Bennett et al. 2013; Planck Collaboration X 2016; Remazeilles et al. 2018). To generate the Commander confidence mask, we use  $5^\circ$  FWHM beam smoothed synchrotron Stokes  $Q_{\nu_0}^s$  and  $U_{\nu_0}^s$  template maps at reference frequency  $\nu_0 = 30$  GHz and extrapolate to 75 GHz using a power-law spectrum with  $\beta_s = -3.0$ . Next we compute the polarization intensity,  $P^s = \sqrt{(Q_{75}^s)^2 + (U_{75}^s)^2}$ , from the extrapolated Stokes  $Q$  and  $U$  maps and mask pixels where  $P^s$  is greater than 2 - 6 times

of  $0.16 \mu\text{K}$ . The reference cutoff of  $0.16 \mu\text{K}$  is the r.m.s fluctuations of the CMB polarization intensity map smoothed at  $5^\circ$  FWHM. The dust polarization intensity thresholds is determined in the similar fashion by extrapolating 353 GHz GNILC dust map to 75 GHz using the MBB spectrum with a fixed  $T_d = 19.4\text{K}$  and  $\beta_d = 1.6$ . We use the same to define the dust masks. The final mask is constructed from the union of the dust and synchrotron masks. The left panel of Fig. 5, shows the set of Galactic mask used for SET1a that retains 30 - 70 % sky fraction. The regions shown in brown colors of different shades are masked out to retain different sky fraction.

Similarly, we prepare the Galactic mask for the sky configuration SET3a-b at  $N_{\text{side}} = 128$  by choosing the threshold of  $0.48 \mu\text{K}$ , which is three times the r.m.s fluctuations of the CMB polarization intensity map smoothed at  $5^\circ$  FWHM. The analysis mask is displayed in the middle panel of Fig. 5 that retains 24 % of the sky.

The NILC confidence masks are constructed by examining the foreground residuals present in the recovered CMB  $B$ -mode map. We prepare the foreground residual  $B$ -mode map by propagating the NILC weights obtained from the analysis of the total frequency maps to foreground maps only at ECHO frequencies. We square the foreground residual map, smoothed it to  $9^\circ$  FWHM beam resolution, and choose appropriate threshold values to retain 20 % to 80 % of the total sky fraction. The set of NILC masks used for the analysis of sky configuration SET1a are displayed in the right panel of Fig. 5. The different brown shaded regions are masked out for retaining different sky fractions.

### 4.3 Power spectrum estimation and Likelihood Analysis

We compute the  $BB$  power spectra cross-correlating the recovered  $B$ -mode CMB maps for HM1 and HM2 over the masked sky and then apply the power spectrum based likelihood approach to estimate  $r$ . We apply pseudo- $C_\ell$  estimator (Hivon et al. 2002) from NaMaster code<sup>10</sup> (Alonso et al. 2019). We use apodized mask following Gaussian apodization scheme with FWHM =  $1^\circ$ . NILC returns directly the foreground cleaned CMB  $B$ -mode maps. For Commander, we first decompose the full-sky foreground cleaned CMB  $Q$  and  $U$  maps to full-sky  $E$ - and  $B$ -mode maps and then use only the  $B$ -mode maps in order to avoid the leakage from  $E$ - to  $B$ -modes over the masked sky. We adopt the constant binning scheme of band width  $\Delta\ell = 9$  and  $(2\ell+1)$  weighted band power in  $k^{\text{th}}$  band given by

$$\hat{C}_k^{BB} = \sum_{\ell_{\text{min}}(k)}^{\ell_{\text{max}}(k)} \frac{(2\ell+1)}{\sum_{\ell=\ell_{\text{min}}(k)}^{\ell_{\text{max}}(k)} (2\ell+1)} C_\ell^{BB}, \quad (9)$$

where  $C_\ell^{BB}$  is the unbinned cross power spectrum (hereafter, by  $C_\ell^{BB}$ , we will indicate band power). For simulations in SET3a and SET3b, Commander is applied over the masked sky. To avoid the issue of  $E$ -to- $B$  leakage over the masked sky, we adopt the pure- $B$  estimator implemented in the NaMaster code which minimizes the leakage with additional sample variance (Smith 2006).

Next, we pass the estimated the binned power spectra to the log-likelihood,

$$-2\ln\mathcal{L} = \text{constant} + \sum_{k,k'} \left[ \hat{C}_k^{BB} - C_k^{BB,model}(r, A_L) \right] \Sigma_{k,k'}^{-1} \left[ \hat{C}_{k'}^{BB} - C_{k'}^{BB,model}(r, A_L) \right], \quad (10)$$

where  $k, k'$  indicate the bands and  $\Sigma_{k,k'}$  is  $BB$  band covariance matrix. The band covariance matrix is estimated following similar binning scheme as in Equation 9,

$$\Sigma_{k,k'} = \frac{\sum_{\ell=\ell_{\text{min}}(k)}^{\ell_{\text{max}}(k)} \sum_{\ell'=\ell'_{\text{min}}(k)}^{\ell'_{\text{max}}(k)} (2\ell+1)(2\ell'+1) \Xi_{\ell\ell'}^{BB, BB}}{\sum_{\ell=\ell_{\text{min}}(k)}^{\ell_{\text{max}}(k)} \sum_{\ell'=\ell'_{\text{min}}(k)}^{\ell'_{\text{max}}(k)} (2\ell+1)(2\ell'+1)} \quad (11)$$

where  $\Xi_{\ell\ell'}^{BB, BB}$  (Tristram et al. 2005) is the  $BB$  covariance matrix estimated using NaMaster code. In order to take into account the impact of residual foreground and noise in covariance matrix, we consider both auto- and cross-power spectra in covariance matrix estimation.

We assume, at likelihood level,  $BB$  power spectra can be expressed as combination of theoretical tensor and lensing modes as,

$$C_k^{BB,model}(r, A_L) = \frac{r}{0.01} C_k^{BB,tensor}(r = 0.01) + A_L C_k^{BB,lensing}, \quad (12)$$

where the reference tensor power spectrum,  $C_k^{BB,tensor}$  at  $r = 0.01$  and lensing power spectrum,  $C_k^{BB,lensing}$  are held fixed to baseline  $\Lambda\text{CDM}$  model parameters (Planck Collaboration IV 2018). The reference  $C_\ell$ s are binned using same weighting scheme shown in Equation 9. We assume that impact of delensing can be compressed to a single scale invariant parameter  $A_L$ . We fix  $A_L = 1$  (for no delensing) and 0.16 (for 84 % delensing) in Equation 12 while estimating the maximum probable value  $r_{mp}$  and its uncertainty  $\sigma(r_{mp})$ . By maximising the log-likelihood given in Equation 10, we analytically estimate the best-fit value of  $r_{mp}$  given by,

$$r_{mp} = 0.01 \times \frac{\sum_{k,k'} \left[ \hat{C}_k^{BB} - A_L C_k^{BB,lensing} \right] \Sigma_{k,k'}^{-1} C_{k'}^{BB,tensor}}{\sum_{k,k'} \left[ \hat{C}_k^{BB,tensor} \Sigma_{k,k'}^{-1} C_{k'}^{BB,tensor} \right]}. \quad (13)$$

We can compute the Fisher matrix using  $F_{ij} = -\left\langle \frac{\partial^2 \ln\mathcal{L}}{\partial\theta_i \partial\theta_j} \right\rangle$  ( $r$  and  $A_L$  are denoted by general notation  $\theta$ ) evaluated at best-fit parameters. The  $1\sigma$  error bar of the parameters are given by  $\sqrt{F_{ii}^{-1}}$ . Using Equation 10 in Fisher matrix, we obtain the  $1\sigma$  error bar of  $r_{mp}$  as,

$$\sigma(r_{mp}) = 0.01 \times \sqrt{\left[ \hat{C}_k^{BB,tensor} \Sigma_{k,k'}^{-1} C_{k'}^{BB,tensor} \right]^{-1}}. \quad (14)$$

## 5 FORECAST RESULTS

The recovered CMB maps obtained using Commander and NILC are expected to contain residuals of foreground and instrumental noise. In case of polarization of CMB, the level of the residual can be high enough to largely bias the measurement of angular power spectra depending on foreground complexity and hence the measurement of tensor-to-scalar

<sup>10</sup> <https://github.com/damonge/NaMaster>

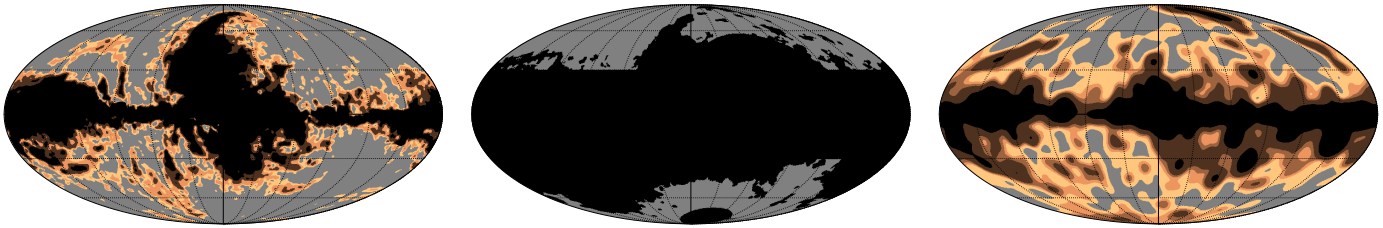


**Figure 5.** Left panel: Series of Galactic mask used analysis of CMB map recovered from **Commander** for SET1a. The region shown in *darkest brown* is masked out to retain 70 % sky. The regions shown in increasingly fainter *brown* colors are incrementally masked out regions, corresponding in turn to retain 60 %, 50 %, 40 % and 30 % sky fractions respectively. Middle panel: Galactic mask comprising 24 % sky fraction at  $N_{\text{side}} = 128$  that is used in analysis of recovered CMB maps from **Commander** for SET3a-b simulations. The region shown in *darkest brown* color is masked out. Right panel: NILC Galactic masks for  $B$ -mode for SET1a simulation. The *darkest brown* region masks 20 % of the sky. The regions with increasingly fainter *brown* colors mask out 40 %, 50 %, 60 % and 80 % of the sky respectively.

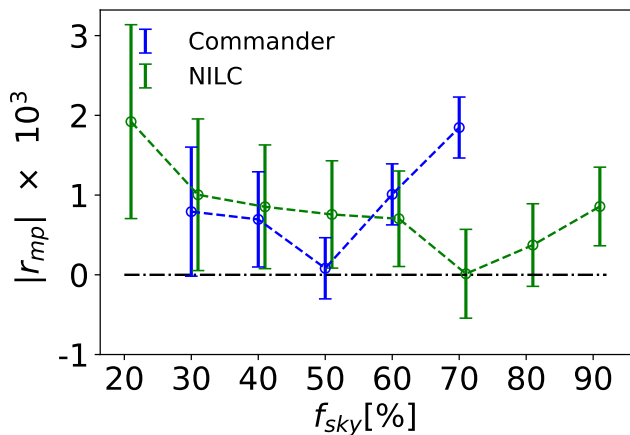


**Figure 6.** The changes in  $r$  bias and uncertainty estimated from foreground cleaned CMB maps by **Commander** (*blue*) and **NILC** (*green*) with different sky fractions for simulation in SET1a. Black dashdotted line is input  $r = 0$ . The  $r$  bias reduces with reducing sky fraction with the cost of small degradation of  $r$  sensitivity up to  $f_{\text{sky}} = 50$  % (for **Commander**) and 70 % (for **NILC**). Further reduction of sky fraction introduces larger bias due to loss of information at large angular scales.

ratio. Lensing  $B$ -mode of CMB adds to this complication because it appears as nuisance to primordial  $B$ -mode of CMB. In this section, we discuss the impact of foreground residuals on biasing  $r$  measurement for various complexity of the foreground models and lensing corrections.

## 5.1 Map based results

### 5.1.1 Effect of sky coverage

Finding an optimal Galactic mask is very critical for our work as the level of the residuals of foreground for  $B$ -mode is not only high in the Galactic plane but also significant in the upper and lower Galactic plane. We experiment with different sets of Galactic masks retaining sky fraction ranging from 90% and to 20% (see Fig. 5). Fig. 6 shows the impact of the different Galactic masks on the measurement of tensor-to-scalar ratio for the simulations without AME and point sources (SET1a). The results clearly show that the bias in the measurement of  $r$  ratio is minimum for the

**Table 5.** The maximum probable value of  $r$  and its associated uncertainties obtained from the posterior distribution for different choices of  $\ell_{\text{max}}$  cutoff for SET1a. The sky fraction is fixed at 40 % for **Commander** analysis. Uncertainties are consistently improved with addition of power from higher  $\ell$  modes up to  $\ell_{\text{max}} \sim 130$ , since most of the constraining power on  $r$  is localized near recombination bump at  $\ell \sim 100$ .

$\ell_{\text{max}}$	Commander		NILC	
	$r_{\text{mp}} \times 10^3$	$\sigma(r) \times 10^3$	$r_{\text{mp}} \times 10^3$	$\sigma(r) \times 10^3$
24(near reionization bump)	-1.06	0.82	-0.12	1.69
42	-0.77	0.42	1.37	1.13
60	-0.51	0.42	0.24	0.89
78	-0.35	0.40	-0.07	0.77
96(near recombination bump)	-0.15	0.39	-0.26	0.72
114	-0.15	0.39	-0.42	0.69
132	-0.14	0.39	-0.54	0.68
150	-0.11	0.39	-0.56	0.68
180	-0.08	0.39	-0.62	0.68
249	-	-	-0.68	0.67
348	-	-	-0.76	0.68
447	-	-	-0.75	0.67
501	-	-	-0.75	0.67
591	-	-	-0.76	0.67

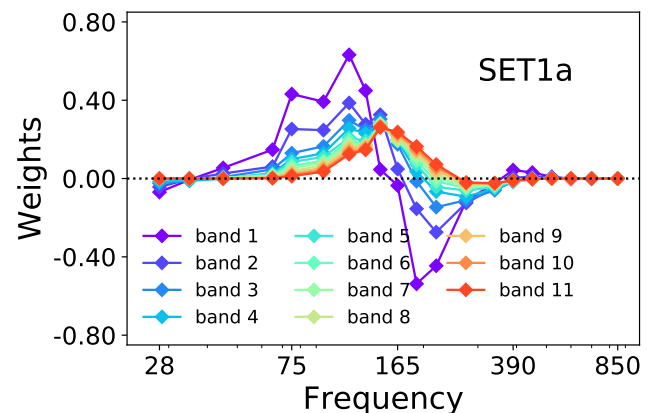


**Figure 7.** Distribution of the full sky average values of the NILC weights across different frequency channels. All the 11 NILC bands have been displayed in the figure for the SET1a sky model.

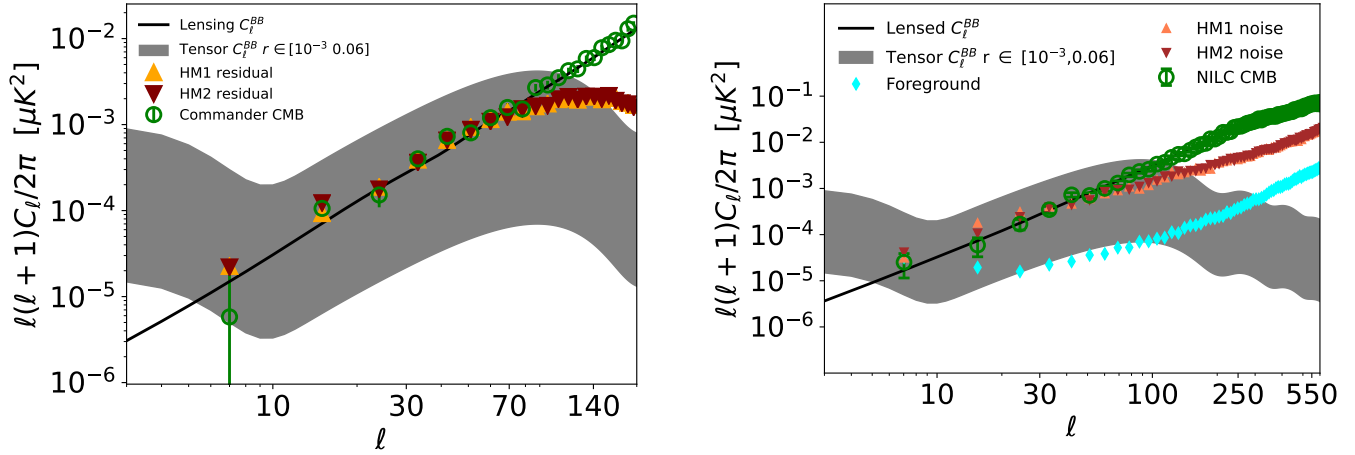


**Figure 8.**  $BB$  cross-power spectra (green circles) estimated over 50% & 70% sky fraction from HM1, HM2 recovered maps using Commander (left panel) & NILC (right panel) respectively for configuration SET1a. The  $1\sigma$  error bars are the quadratic sum of cosmic variance of CMB  $C_{\ell}$  and uncertainty introduced by residual noise and foregrounds as estimated by NaMaster. Black solid line is the theoretical lensed  $BB$  power spectrum, grey-shaded region is theoretical tensor  $BB$  power spectra for range of  $r \in [10^{-3}, 0.06]$ . Contribution of foreground + noise residual leakage to two half-mission maps recovered by Commander are shown in orange and maroon triangles. For NILC, the residual foreground (cyan diamonds) and noise power spectra for two half-missions (HM1 in maroon and HM2 in orange) are displayed for reference.

**Table 6.** Results of maximum likelihood estimation of  $r$  from  $BB$  power spectrum estimated from foreground-cleaned maps using NILC and Commander pipelines. We list best-fit foreground bias on  $r$ ,  $1\sigma$  uncertainties and  $\chi^2/\text{dof}$  for different foreground setups.

Sim.ID	NILC			Commander		
	$r_{mp} \times 10^3$	$\sigma(r_{mp}) \times 10^3$	$\chi^2/\text{dof}$	$r_{mp} \times 10^3$	$\sigma(r_{mp}) \times 10^3$	$\chi^2/\text{dof}$
SET1a	-0.76	0.67	0.60	-0.08	0.39	0.95
SET1b	-0.55	0.68	0.61	0.17	0.38	0.92
SET1c	0.81	0.71	0.74	0.52	0.40	1.02
SET1d	-0.49	0.33	0.54	0.44	0.17	0.57
SET1e	0.34	0.81	0.89	0.92	0.43	0.99
SET1f	0.54	0.78	0.92	3.38	0.55	0.69
SET2a	1.57	1.10	1.11	47.45	1.48	33.7
SET2b	0.62	1.19	1.91	51.06	1.56	33.9
SET2c	1.09	1.16	1.90	34.82	1.43	25.5
SET3a	-	-	-	1.35	0.69	4
SET3b	-	-	-	188.41	5.93	123

mask that retains the sky fraction 70% for NILC and 50% for Commander. We notice that optimum sky fraction remains same for Commander while that reduces to 50% for NILC with addition of AME and point sources in simulation (SET1c).

### 5.1.2 Impact of $\ell_{max}$ cut-off

In Table 5, we summarize the dependency of  $r_{mp}$  and  $\sigma(r)$  as a function of maximum  $\ell$  cut-off ( $\ell_{max}$ ) in the likelihood analysis for the sky configuration SET1a. Since most of the power for constraining  $r$  is concentrated at  $\ell \lesssim 120 - 150$ , we find the  $\sigma(r)$  improves consistently up to  $\ell_{max} \sim 130$ . Further

addition of power from the higher  $\ell$  modes does not improve  $\sigma(r)$ . For our forecast results, we use the information of full range of available  $\ell$  values:  $2 \leq \ell \leq 180$  for Commander and  $2 \leq \ell \leq 600$  for NILC.

### 5.1.3 Forecast results for baseline foreground model

We begin our investigation with the results for our baseline sky configuration SET1a. In the foreground components, we only consider the polarized thermal dust with a single MBB spectrum and polarized synchrotron that follows the GALPROP scaling. In Fig. 7 we display the full sky average



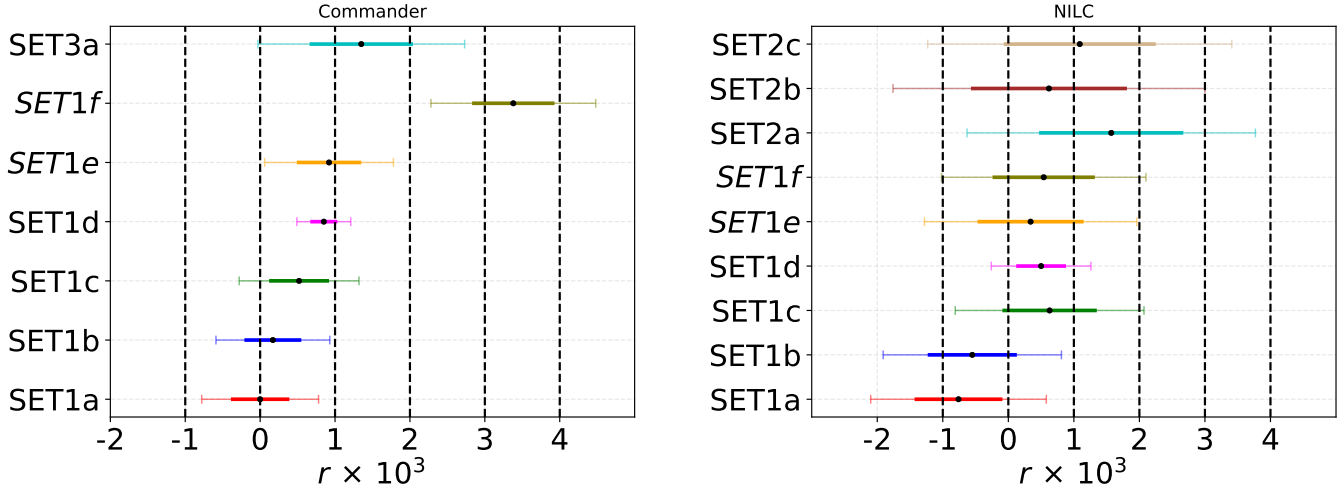


**Figure 9.** The figure depicts the maximum likelihood values of  $r$  (black dots),  $1\sigma$  (thick lines) and  $2\sigma$  (thin lines) error bars for different sky configurations as listed in Table 3 for Commander (left panel) and NILC (right panel) pipelines. Vertical black dashed lines are drawn at  $r = \{-1, 0, 1, 2, 3, 4\} \times 10^{-3}$ . The  $r_{mp}$  values are consistent with null detection within their  $2\sigma$  limit for all sky configurations except for curved-power law synchrotron (SET1f) in case of Commander. Note that, we do not include the results for SET2a-c and SET3b for Commander as the foreground residuals are significantly high due to the mismatch between the data model we fit and the sky model in presence of dust decorrelation. The corresponding results are listed in Table 6.

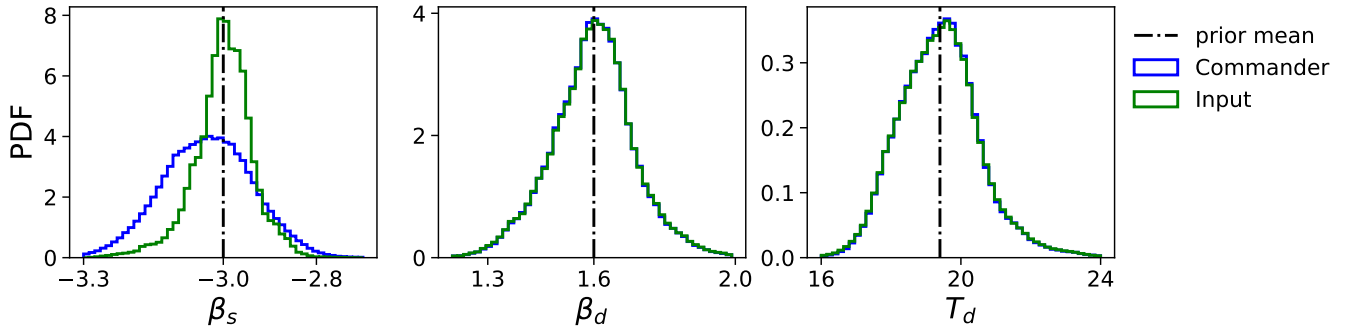


**Figure 10.** Comparison between probability density function (PDF) of Commander estimated foreground spectral parameters (blue) and corresponding input spectral parameters (green) for configuration SET1e. Left panel: PDF of synchrotron spectral index  $\beta_s$ , Middle panel: PDF of dust spectral index  $\beta_d$  and Right panel: PDF of thermal dust temperature  $T_d$ . The black dash-dotted vertical lines are the corresponding mean values of Gaussian prior adopted.

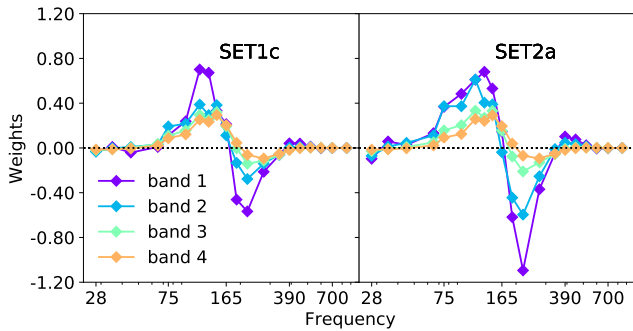


**Figure 11.** Distribution of the full sky average values of the NILC weights in the first four bands, across the ECHO frequency channels for SET1c (left panel) and SET2a (right panel) sky configurations.

values of NILC weights at 11 Needlet bands for all frequency channels. Inspecting the NILC weights, we find that most of the contribution in the final reconstruction of the CMB map comes from the frequency channels between 65 to 340 GHz. As foreground is the main contaminant at larger scales, the first four NILC band weights largely drives the minimization of the foreground and changes significantly for different foreground models. At small angular scales, where noise is the dominant contaminant, we can see from the weights that even fewer frequency channels (115–190 GHz) contribute in the reconstruction of CMB.

We estimate the  $BB$  cross-power spectra over optimal masks (see Section 5.1.1) from the foreground cleaned two half-mission maps and use them in the likelihood analysis. In Fig. 8, we present the estimated  $BB$  cross-power spectra from recovered CMB maps from Commander (left panel) and NILC (right panel). The contributions of leakage from

the foreground and noise to the cleaned CMB  $B$ -mode map are also shown for reference. Residual leakage has significant contribution in resulting power spectra mainly at low  $\ell$  ( $< 60$ ).

The estimated  $r$  bias are consistent with the null detection at the level of  $1\sigma$ . It implies that the residual foreground and noise does not introduce significant bias in the estimation of  $r$  for the baseline simulation. However, the foreground residuals inflate the associated uncertainties on  $r$  to  $0.79 \times 10^{-3}$  and  $0.39 \times 10^{-3}$  for NILC and **Commander** respectively which correspond to 75 % and 49 % increment as compared to the analytic forecast results with the idealised assumption of no foregrounds. The analytic forecast results rely on Fisher matrix formula:

$$\sigma(r) = 0.01 \left\{ \sum_{\ell_{\min}}^{\ell_{\max}} \frac{(2\ell+1)f_{\text{sky}}}{2} \left[ \frac{C_{\ell}^{BB, \text{tensor}}(r=0.01)}{C_{\ell}^{BB, \text{lensing}} + N_{\ell}^{BB}} \right]^2 \right\}^{-1/2},$$

where we consider ECHO noise power spectra  $N_{\ell}^{BB}$  as shown in Fig. 1. It implies that the uncertainty on the estimation of  $r$  is mostly dominated by the foreground residuals even for the simplest assumptions about the polarized foreground emissions.

Table 6 summarizes the estimated values of maximum probable  $r$  and  $1\sigma$  uncertainties for all the set of simulations considered in our analysis. To check for any possible bias present in the two component separation pipelines, we rerun the same analysis for independent set of CMB and noise realization for SET1a (keeping the foreground maps fixed). We report the maximum probable value of  $r$  as  $(-0.54 \pm 0.41) \times 10^{-3}$  (COMMANDER) and  $(-0.15 \pm 0.82) \times 10^{-3}$  (NILC). These results imply that the two component separation pipelines are unbiased and the estimated maximum probable values of  $r$  reported in Table 6 is due to the statistical fluctuation for a particular CMB and noise realization. In order to check the goodness of fitting of power spectra, we also have listed  $\chi^2$  per degrees of freedom (dof) in Table 6. In Fig. 9, we show a comparison of  $r_{mp}$  (black dots) along with  $1\sigma$  (thick lines) and  $2\sigma$  (thin lines) uncertainty for our baseline simulation with some other set of simulations.

#### 5.1.4 Effect of polarized AME and faint point sources

The sky configurations SET1b and SET1c have been generated from the baseline configuration by adding respectively the polarized AME and AME, extragalactic faint point sources consistent with the current upper limits. Since NILC is a blind component separation method, it adjusts the weights to minimize this extra complication of the sky. As far as the analysis of these sky using **Commander** is concerned, we have ignored the polarized AME and extragalactic point sources component while fitting the foreground model within the **Commander** pipeline. While the results show that the polarized AME component does not introduce any significant bias (consistent with null detection within  $1\sigma$ ) in the measurement of  $r$  (see Table 6 for reference), the extragalactic faint point sources exhibit a small bias (null detection within  $\sim 2\sigma$ ) in the measure of  $r$  even after applying very conservative mask of sky fraction 50%.

#### 5.1.5 Delensing assessment

In our forecast, we explore the possibility of improvement of sensitivity of  $r$  measurement with one possible scenarios of

delensing with 84 % reduction of lensing power. We explore this scenario in sky configuration SET1d. In this configuration, we adopt the same foreground model as SET1a. The estimated value is  $r = (-0.49 \pm 0.33) \times 10^{-3}$  and  $(0.44 \pm 0.17) \times 10^{-3}$  for NILC and **Commander** respectively. The results show an improvement of  $\sigma(r)$  by  $\sim 50\%$  as compared to the results for same foreground configuration without delensing in SET1a.

#### 5.1.6 Departures from baseline model: synchrotron and dust complexity

In this section, we explore the set of sky configurations with different synchrotron emission laws and dust templates. We fix the model of polarized AME and point sources as used in SET1c.

*Synchrotron scaling* - We update the emission law of polarized synchrotron from the GALPROP scaling relation to the power-law and curved power-law behaviour in the sky configurations SET1e and SET1f respectively. For NILC, the  $r$  bias for the synchrotron power-law and curved power-law models are consistent with the GALPROP scaling relation with a marginal increment of  $\sigma(r)$ . For both sets, and the values of  $r_{mp}$  are consistent with the null detection within  $2\sigma$ .

In **Commander** parameterization, we fit synchrotron by same spectral scaling as used in these two respective sky configurations. We find that  $\sigma(r)$  increases marginally in comparison to same for GALPROP scaling. Furthermore, both the scaling introduce significantly larger bias for **Commander** as compared to NILC. For power-law scaling, although bias is consistent with zero within  $3\sigma$  limit, for curved power-law scaling, the bias is too large to be consistent with zero within  $3\sigma$ . This additional bias on  $r$  for **Commander** is attributed to lack of frequency channels in low frequency side of the spectrum. In Fig. 10, we compare the distribution of input and **Commander** recovered maps of synchrotron spectral index,  $\beta_s$  (left panel), dust spectral index,  $\beta_d$  (middle panel), and dust temperature,  $T_d$  (right panel) used in simulation in SET1e. We find **Commander** fits thermal dust spectral parameters  $T_d$  and  $\beta_d$  with desired accuracy. However, lack of frequency channels  $< 28$  GHz prevents **Commander** to fit synchrotron spectral index adequately. This incorrect fitting to the data at low frequency results in incorrect foreground subtraction and results in a large biased estimation of  $r$ .

*Impact of decorrelation* - The frequency-frequency decorrelation of thermal dust may play a crucial role in introducing larger bias in  $r$  measurement, especially for parametric component separation. To investigate this, we first use three sky configurations SET2a-c where we use MKD - dust model that exhibits decorrelation across the frequencies. Three different synchrotron scaling are adopted in these three configurations. In Fig. 11 we compare the NILC weights for configurations SET1c and SET2a which exhibit simple dust and decorrelated dust model respectively. We find that to account for complexity in dust modelling the NILC pipeline assigns higher weights to the first three Needlet bands. However, the level of residuals is still significantly higher as compared to configuration with simple dust model. This is clearly demonstrated in Fig. 12 where we compare the power spectra of residual noise and foreground for configurations SET1c and SET2a. The decorrelated thermal dust model in SET2a exhibits larger residual at large angu-

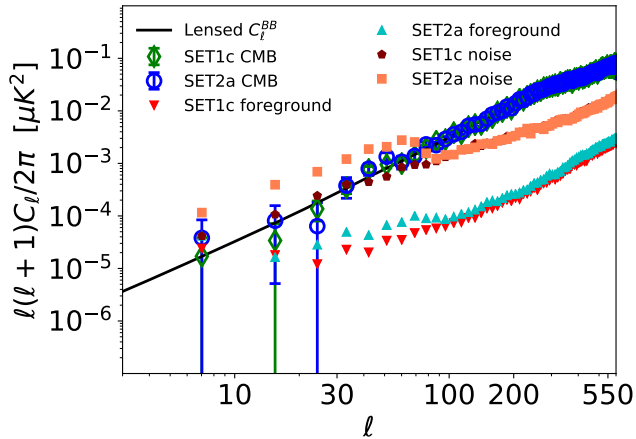


**Figure 12.** Comparison of NILC recovered CMB  $BB$  power spectra for a single layer GNILC dust model used in SET1c (*green diamond*) and six-layers MKD – dust dust model used in SET2a (*blue circle*). The other foreground components are same for both the sky configurations. The foreground and noise residuals are also compared for two simulations.

lar scales. As a result, the bias in  $r$  increases by two-times and the uncertainty increases by 33%.

The forecast results for **Commander** show a very strong  $r$  bias in comparison to the same for configurations in absence of dust decorrelation. This happens because the parametric component separation depend on whether the decorrelation across the ECHO frequencies is properly parameterized in the dust model. Here, we consider one component MBB for fitting thermal dust in **Commander** that does not parameterize dust decorrelation. Because of incorrect assumption in dust modelling, we are effectively allowing the spectral mismatch between simulated dust in data and the model of the dust in parametric separation. Clearly this mismodelling of dust spectral property leaves a spurious dust residual in **Commander** recovered CMB maps resulting in a strong  $r$  bias.

In order to investigate the impact of mismodelling in a more comprehensive manner, we consider two more simulations in configurations SET3a and SET3b where we introduce TD – dust template. In SET3a, we do not introduce decorrelation whereas dust in SET3b exhibits decorrelation. We fit dust in both the configurations with one-component MBB spectrum. For SET3a, we find expected  $r$  bias, since **Commander** does not suffer from mismodelling. However, for SET3b, we find a extremely large bias due to decorrelated dust, being attempted to be fit by a simple one-component MBB dust model. This implies adequate dust subtraction in presence of decorrelation is not possible with this simplest approach in the version of **Commander** used here. We require different parameterization or multi-layer dust model in parametric separation to mitigate decorrelated dust.

We report the quality of fitting of model power spectrum to estimated  $C_\ell$  in Table. 6 measuring  $\chi^2/d.o.f$ . We find  $\chi^2/d.o.f$  values are close to one for NILC pipeline except for the cases where we use decorrelated dust (SET2a-c). The decorrelated dust introduces excess bias at  $\ell$  below 100 that prevents good fitting to the model power spectrum. For **Commander** the  $\chi^2/d.o.f$  is close to one for the cases where there is no mismatch between data and foreground model (SET1a-e). Conversely, for SET1f, estimated  $r$  has bias and

$\chi^2/d.o.f$  is close to the baseline value because although the fitting to estimated  $C_\ell$  is good, bias is due to the lack of frequency coverage of this experiment. The departure of  $\chi^2$ -values from baseline value for SET2a-c and 3b is due to the incorrect of dust model used in **Commander**. The estimated  $r$  has bias and  $\chi^2$  value is comparatively large for SET3a probably because we do not have access to the angular scales below  $\ell = 40$  for this simulation where the reionization peak is present.

## 6 CONCLUSIONS

In this paper, we study whether instrument specification of ECHO allows us efficient foreground subtraction to detect the primordial  $B$ -mode polarization in CMB to reach its scientific goal. Two component separation pipelines NILC and **Commander** have been applied to set of foreground configurations covering a range of complexity over ECHO channels followed by the power-spectrum estimation and likelihood analysis. This allows us to study ability of foreground subtraction of the pipelines for ECHO instrument design through fully propagating the foreground residuals in estimation of  $r$  sensitivity. Our simulations consist of dust and synchrotron with varying complexity, and two additional components due to polarized AME and point sources. The impact of gravitational lensing has also been tested comparing forecast results introducing fully lensed and 84% delensed CMB maps.

If there is no spectral mismatch between simulated components in the data and parametric model fitting to the data, **Commander** can constraint  $r$  for larger than  $3 \times 10^{-3}$  at  $3\sigma$ . However, we find need for more frequency channels at the low-frequency end of the spectrum to fit the power-law and curved power-law synchrotron. The blind component separation NILC can constraint  $r$  for larger than  $2 \times 10^{-3}$  at  $3\sigma$ . If 84% delensing is possible to be achieved, we find the sensitivity can be improved by 50% independent of component separation pipeline. The AME and point sources have a negligible impact on the sensitivity of  $r$  measurement.

The **Commander** version used in this work cannot fit spectral parameters of dust adequately for the decorrelated dust model and hence subtracts foregrounds inadequately which results in immense bias on  $r$ . Therefore ECHO cannot achieve its desired sensitivity with current **Commander** framework in presence of decorrelation. We argue that we should not ignore the modelling of decorrelation/multi-component dust in parametric foreground subtraction for such a high sensitive instrument. Since NILC is a blind component separation, decorrelation does not deteriorate its performance much. However, decorrelation introduces larger residual leakage at large scale for NILC that results in increment of  $\sigma(r)$  by a factor of  $\sim 1.5$  in comparison to same in absence of decorrelation. We anticipate that impact of decorrelated dust may be possible to mitigate using some alternative approach of foreground separation, e.g. moment expansion based component separation algorithms (Chluba et al. 2017; Ichiki et al. 2019; Remazeilles et al. 2020; Adak 2021; Rotti & Chluba 2021)

A number of potential sources of systematic errors due to instrument imperfections and miscalibration are not considered in this paper. The treatment of those, and their possible interaction with the foreground cleaning algorithms, is

left to future work. Another source of bias in our analysis comes from the Gaussian approximation of the likelihood function defined in Equation 10. At low multipoles ( $\ell < 30$ ), the likelihood function of the power spectrum is slightly non-Gaussian (Verde et al. 2003; Hamimeche & Lewis 2008). We will address the potential bias in  $r$  estimation due to this effect in our forthcoming paper.

## ACKNOWLEDGEMENTS

DA acknowledges the University Grants Commission India for providing financial support as Senior Research Fellow. This work was supported by Science and Engineering Research Board, Department of Science and Technology, Govt. of India grant number SERB/ECR/2018/000826. All the computation using **Commander** code in this paper are done on the Pegasus cluster<sup>11</sup> at IUCAA. The results in this paper have been derived using the **HEALPix** package. DA acknowledges Prof. Hans Kristian Eriksen and Dr. Ranajoy Banerji for helping to install **Commander** and preparing the parameter files. DA also acknowledges Dr. Shabbir Shaikh for useful discussion. AS acknowledges the use of Padmanabha cluster<sup>12</sup> at IISER-TVM for her work. AR acknowledges support from the ERC Consolidator Grant CMBSPEC (No. 725456) as part of the European Union’s Horizon 2020 research and innovation program.

## DATA AVAILABILITY

No external data are analysed in support of this research. The data will be shared on reasonable request to the corresponding author.

## References

- Abazajian K., et al., 2022, *The Astrophysical Journal*, 926, 54
- Adak D., 2021, *Monthly Notices of the Royal Astronomical Society*, 507, 4618
- Adak D., Ghosh T., Boulanger F., Haud U., Kalberla P., Martin P. G., Bracco A., Souradeep T., 2020, *A&A*, 640, A100
- Ade T. P. C. P. A. R., et al., 2014, *The Astrophysical Journal*, 794, 171
- Ade P. A. R., et al., 2021, *Phys.Rev.Lett*, 127, 151301
- Aghanim N., et al., 2020, *Astronomy & Astrophysics*, 641, A1
- Aiola S., et al., 2020, *Journal of Cosmology and Astroparticle Physics*, 2020, 047
- Akrami Y., et al., 2020, *Astronomy & Astrophysics*, 641, A10
- Albrecht A., Steinhardt P. J., 1982, *Phys. Rev. Lett.*, 48, 1220
- Ali-Haïmoud Y., Hirata C. M., Dickinson C., 2009, *Monthly Notices of the Royal Astronomical Society*, 395, 1055
- Alonso D., Dunkley J., Thorne B., Naess S., 2017, *Phys. Rev. D*, 95, 043504
- Alonso D., Sanchez J., Slosar A., LSST Dark Energy Science Collaboration 2019, *MNRAS*, 484, 4127
- André P., et al., 2014, *Journal of Cosmology and Astroparticle Physics*, 2014, 006
- Baleato Lizancos A., Challinor A., Sherwin B. D., Namikawa T., 2021, arXiv e-prints, p. arXiv:2102.01045
- Basak S., Delabrouille J., 2012, *Monthly Notices of the Royal Astronomical Society*, 419, 1163
- Basak S., Delabrouille J., 2013, *Monthly Notices of the Royal Astronomical Society*, 435, 18
- Bennett C. L., et al., 2013, *ApJS*, 208, 20
- Bonavera L., González-Nuevo J., Argüeso F., Toffolatti L., 2017, *MNRAS*, 469, 2401
- Bull P., et al., 2016, *Physics of the Dark Universe*, 12, 56
- Chluba J., Hill J. C., Abitbol M. H., 2017, *MNRAS*, 472, 1195
- Choi S. K. e. a., 2020, arXiv e-prints, p. arXiv:2007.07289
- Delabrouille, J. et al., 2013, *A&A*, 553, A96
- Delabrouille J., Cardoso J. F., Le Jeune M., Betoule M., Fay G., Guilloux F., 2009, *A&A*, 493, 835
- Delabrouille J., et al., 2018, *JCAP*, 2018, 014
- Delabrouille J., et al., 2019, arXiv e-prints, p. arXiv:1909.01591
- Dickinson C., Peel M., Vidal M., 2011, *Monthly Notices of the Royal Astronomical Society: Letters*, 418, L35
- Dunne L., Eales S., Edmunds M., Ivison R., Alexander P., Clements D. L., 2000, *Monthly Notices of the Royal Astronomical Society*, 315, 115
- Eriksen H. K., Banday A. J., Górski K. M., Lilje P. B., 2004, *ApJ*, 612, 633
- Eriksen H. K., Jewell J. B., Dickinson C., Banday A. J., Górski K. M., Lawrence C. R., 2008, *ApJ*, 676, 10
- Errard J., Feeney S. M., Peiris H. V., Jaffe A. H., 2016, *JCAP*, 2016, 052
- Fauvet, L. et al., 2011, *A&A*, 526, A145
- Finkbeiner D. P., 2004, *ApJ*, 614, 186
- Ghosh T., et al., 2017, *A&A*, 601, A71
- Green G. M., et al., 2015, *ApJ*, 810, 25
- Gualtieri R., et al., 2018, *Journal of Low Temperature Physics*, 193, 1112
- Guth A. H., 1981, *Phys. Rev. D*, 23, 347
- Génova-Santos R., et al., 2015, *Monthly Notices of the Royal Astronomical Society*, 452, 4169
- Hamimeche S., Lewis A., 2008, *Phys.Rev.D*, 77, 103013
- Hanany S., et al., 2019, arXiv e-prints, p. arXiv:1902.10541
- Haslam C. G. T., Salter C. J., Stoffel H., Wilson W. E., 1982, *A&AS*, 47, 1
- Hazumi M., et al., 2019, *J. Low Temp. Phys.*, 194, 443
- Hivon E., Gorski K. M., Netterfield C. B., Crill B. P., Prunet S., Hansen F., 2002, *The Astrophysical Journal*, 567, 2
- Hu W., White M., 1997, *New Astronomy*, 2, 323
- Ichiki K., Kanai H., Katayama N., Komatsu E., 2019, *Progress of Theoretical and Experimental Physics*, 2019, 033E01
- Jeffreys H., 1939, *The Theory of Probability*. Oxford Classic Texts in the Physical Sciences
- Kamionkowski M., Kosowsky A., 1998, *Phys.Rev.D*, 57, 685
- Kazanas D., 1980, *ApJ*, 241, L59

<sup>11</sup> <http://hpc.iucaa.in/>

<sup>12</sup> <https://hpc.iisertvm.ac.in/>



- Knox L., Turner M. S., 1993, *Phys. Rev. Lett.*, 70, 371
- Kogut A., et al., 2007, *The Astrophysical Journal*, 665, 355
- Krachmalnicoff, N. Baccigalupi, C. Aumont, J. Bersanelli, M. Mennella, A. 2016, *A&A*, 588, A65
- Lazarian A., 2007, *J. Quant. Spec. Radiat. Transf.*, 106, 225
- Leitch E. M., Readhead A. C. S., Pearson T. J., Myers S. T., 1997, *ApJ*, 486, L23
- Linde A. D., 1982, *Physics Letters B*, 108, 389
- Manzotti A., 2018, *Phys. Rev. D*, 97, 043527
- Manzotti A., et al., 2017, *ApJ*, 846, 45
- Martínez-Solauche G., Karakci A., Delabrouille J., 2018, *MNRAS*, 476, 1310
- Miville-Deschênes, M.-A. Lagache, G. Boulanger, F. Puget, J.-L. 2007, *A&A*, 469, 595
- Miville-Deschênes M. A., Ysard N., Lavabre A., Ponthieu N., Macías-Pérez J. F., Aumont J., Bernard J. P., 2008, *A&A*, 490, 1093
- Moshir M., Kopman G., Conrow T. A. O., 1992, IRAS Faint Source Survey, Explanatory supplement version 2
- Mukherjee S., Paul S., Choudhury T. R., 2019, *MNRAS*, 486, 2042
- Narcowich F. J., Petrushev P., Ward J. D., 2006, *SIAM Journal on Mathematical Analysis*, 38, 574
- Orlando E., Strong A., 2013, *Monthly Notices of the Royal Astronomical Society*, 436, 2127
- O’Dea D. T., Clark C. N., Contaldi C. R., MacTavish C. J., 2011, *Monthly Notices of the Royal Astronomical Society*, 419, 1795
- Pelgrims, V. Clark, S. E. Hensley, B. S. Panopoulou, G. V. Pavlidou, V. Tassis, K. Eriksen, H. K. Wehus, I. K. 2021, *A&A*, 647, A16
- Planck Collaboration 2014, *A&A*, 571, A11
- Planck Collaboration IV 2018, arXiv e-prints, p. [arXiv:1807.06208](#)
- Planck Collaboration VI 2018, arXiv e-prints, p. [arXiv:1807.06209](#)
- Planck Collaboration X 2016, *A&A*, 594, A10
- Planck Collaboration XI 2020, *A&A*, 641, A11
- Planck Collaboration XLIV 2016, *A&A*, 596, A105
- Planck Collaboration XLVIII 2016, *A&A*, 596, A109
- Planck Collaboration XXV 2016, *A&A*, 594, A25
- Planck Collaboration et al., 2011, *A&A*, 536, A1
- Planck Collaboration et al., 2016, *A&A*, 594, A26
- Puglisi G., et al., 2018, *ApJ*, 858, 85
- Remazeilles M., Delabrouille J., Cardoso J.-F., 2011, *Monthly Notices of the Royal Astronomical Society*, 418, 467
- Remazeilles M., Dickinson C., Eriksen H. K. K., Wehus I. K., 2016, *MNRAS*, 458, 2032
- Remazeilles M., et al., 2018, *JCAP*, 2018, 023
- Remazeilles M., Rotti A., Chluba J., 2020, arXiv e-prints, p. [arXiv:2006.08628](#)
- Ricci, R. Prandoni, I. Gruppioni, C. Sault, R. J. De Zotti, G. 2004, *A&A*, 415, 549
- Rotti A., Chluba J., 2021, *MNRAS*, 500, 976
- Saikia D. J., Salter C. J., 1988, *ARA&A*, 26, 93
- Sato K., 1981, *Monthly Notices of the Royal Astronomical Society*, 195, 467
- Sayre J. T., et al., 2020, *Phys. Rev. D*, 101, 122003
- Seljak U. c. v., Hirata C. M., 2004, *Phys. Rev. D*, 69, 043005
- Seljak U., Zaldarriaga M., 1997, *Phys.Rev.Lett*, 78, 2054
- Sherwin B. D., Schmittfull M., 2015, *Phys.Rev.D*, 92, 043005
- Smith K. M., 2006, *New Astronomy Reviews*, 50, 1025
- Smith K. M., Ferraro S., 2017, *Phys. Rev. Lett.*, 119, 021301
- Starobinsky A., 1980, *Physics Letters B*, 91, 99
- Tegmark M., Efstathiou G., 1996, *MNRAS*, 281, 1297
- The CORe Collaboration et al., 2011, arXiv e-prints, p. [arXiv:1102.2181](#)
- Tristram M., Macías-Pérez J. F., Renault C., Santos D., 2005, *MNRAS*, 358, 833
- Trombetti T., Burigana C., De Zotti G., Galluzzi V., Mas-sardi M., 2018, *A&A*, 618, A29
- Verde L., et al., 2003, *ApJS*, 148, 195
- Wandelt B. D., Larson D. L., Lakshminarayanan A., 2004, *Phys. Rev. D*, 70, 083511
- de Bernardis P., et al., 2018, *Journal of Cosmology and Astroparticle Physics*, 2018, 015
- de Oliveira-Costa A., Tegmark M., Davies R. D., Gutiérrez C. M., Lasenby A. N., Rebolo R., Watson R. A., 2004, *ApJ*, 606, L89